ACS APPLIED POLYMER MATERIALS

Article

Cite This: ACS Appl. Polym. Mater. 2019, 1, 2322−2333

pubs.acs.org/acsapm

Low-Cost, Ambient-Dried, Superhydrophobic, High Strength, Thermally Insulating, and Thermally Resilient Polybenzoxazine Aerogels

Sadeq Malakooti,[†] Guoqiang Qin,[†] Chandana Mandal,[‡] Rushi Soni,[‡] Tahereh Taghvaee,[‡] Yao Ren,[†] Huiluo Chen,[†] Nicholas Tsao,[†] James Shiao,[†] Shameek Sushil Kulkarni,[†] Chariklia Sotiriou-Leventis,[‡] Nicholas Leventis,*[,‡] and Hongbing Lu*[,†]

[†]Department of Mechanical Engineering, The University of Texas at Dallas, Richardson, Texas 75080, United States

[‡]Department of Chemistry, Missouri University of Science and Technology, Rolla, Missouri 65409, United States

Supporting Information

ABSTRACT: A family of ambient-dried polybenzoxazine aerogels is prepared with a facile and scalable process as a high-performance polymeric aerogel with strong and robust thermomechanical properties at elevated temperatures. Those materials are inherently flame-retardant and superhydrophobic over the entire bulk density range (0.24−0.46 g cm^{-3}). In addition, they are mechanically strong with strengths (e.g., 1 MPa at 0.24 g cm^{-3} at room temperature) higher than those of other high-performance aerogels of similar density, including polyimide and polyamide (Kevlar-like) aerogels as well as polymer-cross-linked X-silica and X-vanadia aerogels, at a significantly lower cost. Furthermore, unlike most other glassy polymeric materials, the maximum strength of the synthesized aerogels occurs at service temperatures slightly higher than room temperature (about 50 °C), which eliminates the possibility of any drop in strength with respect to the room temperature strength up to 150 °C at all densities. At higher temperatures (up to 250 °C), the overall performance of those aerogels is also stable and robust without any significant drop in Young's modulus or strength levels, which makes them suitable for various industrial applications including high-performance structural and thermal protection applications as an alternative to the significantly more expensive polyimides.

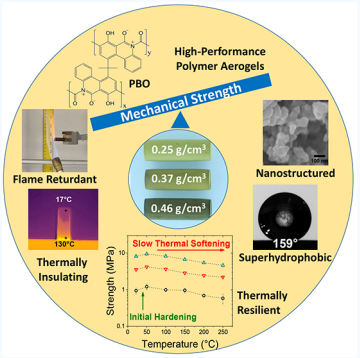

KEYWORDS: *aerogels, polybenzoxazine, high-performance polymers, ambient drying, superhydrophobic surfaces, flame-retardant materials*

1. INTRODUCTION

The quest for ever lighter and stronger high-performance structural materials has been continuously pursued throughout human civilization. With the advent of modern technology, that quest is fundamentally driven by three factors: microstructure (e.g., hierarchical and nanoporous structures), length scale (e.g., size-dependent strengthening), and intrinsic material composition (e.g., the use of metal alloys).[1] However, the limited scalability of nanostructure fabrication processes and the compromised mechanical performance of the resulting materials under harsh environmental conditions are among the main real challenges that affect practical applications.[2−4] Scalable nanomanufacturing approaches such as sol−gel based synthesis along with suitable molding are among the most highly promising methodologies for the preparation of large, low-density, mechanically strong nanostructured materials.[5] In this context, aerogels set amid the low-density materials with synergistic properties such as high specific surface areas and the hierarchical random assembly of nanoparticles.[6] It should be noted that recent novel aerogel synthetic methodologies including nanofiber based assemblies led to low density and large specific surface area aerogels; however, these technologies also rely on several other techniques including sonication induced gelation, electrospinning, or thermal based cross-linking, which essentially increase the manufacturing costs and hinder the scalability.[57,58] These materials can become even more attractive through ambient-drying based sol−gel approaches to reach desirable scalability at low cost.[7−12] Over the past two decades, the mechanical properties of traditional oxide aerogels, e.g., silica, have been dramatically improved by using polymer-cross-linking technologies. The resulting materials are termed X-aerogels.[13−20]

The X-aerogels bear a conformal polymer coating over their entire skeletal framework; the bulk density of the native materials may increase by a factor of 3, but the mechanical properties increase by a factor of 300. Following the success of polymer-cross-linked aerogels, it was reasoned that purely polymeric aerogels with the same nanostructure as X-aerogels should have similar properties. Thus, a new class of purely polymeric aerogel has emerged. Those include aerogels based

Received: April 29, 2019
Accepted: August 2, 2019
Published: August 2, 2019

DOI: 10.1021/acsapm.9b00408
ACS Appl. Polym. Mater. 2019, 1, 2322−2333

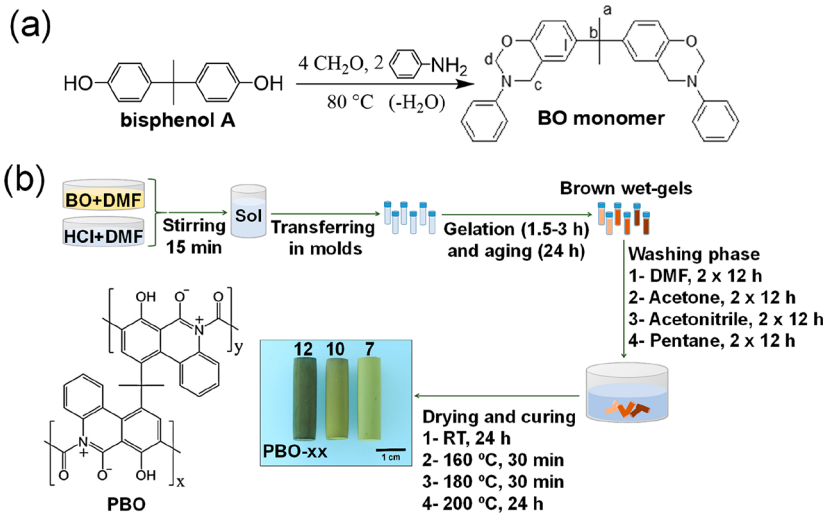

Figure 1. (a) Chemical synthesis of the benzoxazine (BO) monomer. (b) Synthetic protocol of the ambient-dried polybenzoxazine (PBO) aerogels.

on most major polymeric classes such as polyurea,[8,9,21−24] polyurethane,[7,25−30] polyimide,[31] and polyamide (Kevlar-like),[32−34] among many others. The impressive mechanical properties of those aerogels have led to a host of new applications, unthinkable for such low-density materials before, including ballistic armor protection.[35]

As phenolic resins, polybenzoxazines (PBOs) are sturdy with low water retention, and exceptionally high glass transition and decomposition temperatures, which make them an important inexpensive alternative to engineering plastics like polyimides for high-temperature applications.[36] Previous attempts on making PBO aerogels are either accomplished through a high-temperature gelation process (e.g., PBO aerogels synthesized by Lorjai et al.[37,38]) or prepared after a supercritical drying process (e.g., PBO aerogels synthesized by Mahadik-Khanolkar et al.[39,40]) which in both cases, scalability and commercialization, are hindered. It is worth mentioning that in Mahadik-Khanolkar et al.'s approach, the PBO aerogels have been synthesized at room temperature, which is a great advantage for commercialization.[39] Therefore, motivated by their approach, we first became interested in exchanging their PBO aerogel room-temperature supercritical-drying synthetic protocol with a room-temperature ambient-drying approach to contribute further on the scalability of the PBO aerogels. Moreover, with respect to mechanical properties, the previously reported PBO aerogels have not been fully characterized at different environmental and loading conditions. Thus, we systematically studied the fundamental mechanical properties (i.e., both uniaxial and shear properties) of the ambient-dried PBO aerogels under uniaxial compression and pure torsional loading modes with various loading−unloading scenarios at elevated temperatures and different frequencies. To the best of our knowledge, this is the first study of the preparation of room-temperature ambient-dried PBO aerogels with full mechanical characterizations. These investigations will open up the route to the full commercialization of scalable and low-cost PBO aerogels.

2. RESULTS AND DISCUSSION

2.1. Materials Synthesis. The benzoxazine (BO) monomer was synthesized according to our coauthor's previous approach.[39] The BO monomer was prepared from the condensation of bisphenol A, aniline, and formaldehyde (Figure 1a). At room temperature, the PBO wet gels were prepared by using our coauthor's reported HCl-catalyzed process in DMF solvent.[39] However, in this work, the gelation solvent was exchanged repeatedly, from DMF to acetone and then to acetonitrile and finally to pentane. This solvent exchange influences on the inner surface of the gel network which will eventually minimize the capillary forces of the liquid meniscus inside the pore. Then, the wet gels were dried directly from pentane at room temperature under ambient pressure.[41] Three sets of PBO samples at three different BO monomer concentrations (i.e., 7, 10, and 12% w/w) were prepared. The *xx* in PBO-*xx* denotes the monomer concentration. All as-prepared PBO samples were brown (darker at higher monomer concentrations), monolithic, and sturdy. To complete the curing process, all samples were further processed for 24 h at 200 °C in air. As it has been shown previously, that step induces ring fusion of the aniline and the phenolic rings. The PBO sample preparation protocol is summarized in Figure 1b.

2.2. Chemical Characterization. Ring-fusion aromatization of the aniline moiety with the phenolic moiety caused complete disappearance from the FTIR spectra of PBO-*xx* (Figure 2) of both strong absorptions at 747 and 690 cm^{-1} of the BO monomer, which were attributed to the C−H out-of-plane (OOP) bending vibrations of dangling aniline. The Ph−O−C stretches at 1229 cm^{-1} for the BO monomer and the stretches of the cyclic mixed acetal/aminal at 939 cm^{-1} were replaced with a new absorption near 1266 cm^{-1}, which was attributed to the C−O stretching of the dangling phenolic moieties.[39,42] The C−N stretching of the Mannich bridges in the BO monomer, which was observed at 1111 cm^{-1}, became extremely weak in the PBO-*xx* aerogel samples. The absorption at 1183 cm^{-1} corresponded to the Ar−C−Ar stretching in the bisphenol A moiety, and it is also present in the cured sample as expected. The 1700−1750 cm^{-1} region could be related to C═O stretches of carbonyls.

Figure 3 shows the ^{13}C NMR spectra of the BO monomer and of a representative PBO-10 aerogel sample. All the aromatic carbons were observed from 110 to 160 ppm. As expected, the resonances of the $C(CH_3)_2$ bridges between the phenolic moieties survived in the cured polymer, but the

DOI: 10.1021/acsapm.9b00408
ACS Appl. Polym. Mater. 2019, 1, 2322−2333

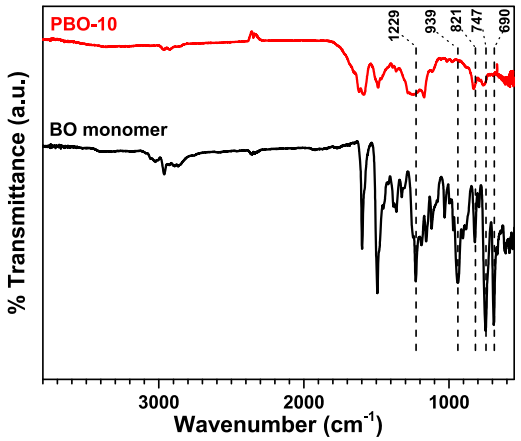

Figure 2. Infrared (FTIR) spectra of the BO monomer and of representative PBO-10 aerogel sample.

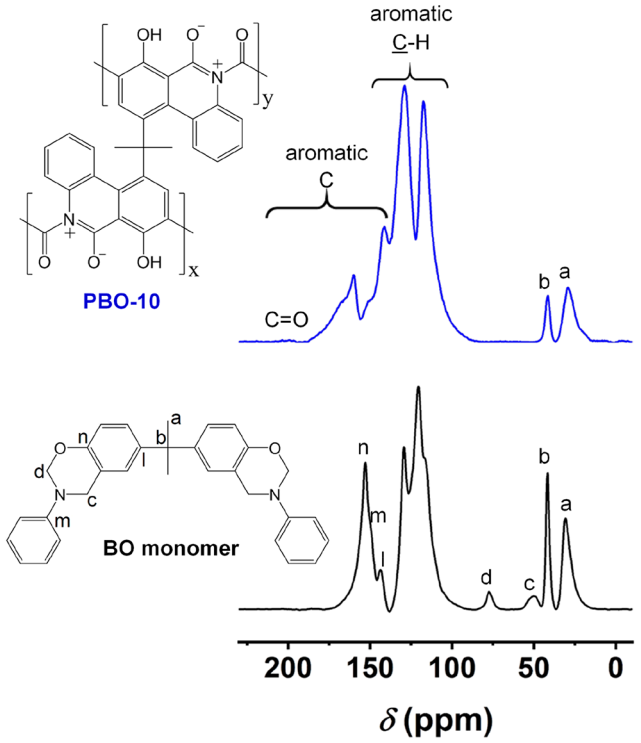

Figure 3. Solid-state CPMAS ^{13}C NMR spectra of the BO monomer and of representative PBO-10 aerogel sample.

resonances of the carbons corresponding to the cyclic mixed acetal−aminal (marked c and d) had disappeared. Those two carbons were oxidized and became part of either a new aromatic phenoxide whose resonances overlaps with the rest of the aromatic resonances or a brand-new carbonyl that gave rise to the weak resonance at around 193 ppm.

2.3. Physical Characterization. *2.3.1. General Material Properties.* The total linear shrinkage of the fully cured PBO aerogels relative to their molds was about 40% (Table 1). The shrinkage of traditional silica gels during aging is caused by dissolution and reprecipitation processes, which are referred to as Ostwald ripening. The latter is not relevant in the case of PBO wet gels, which, therefore showed zero aging shrinkage. Upon solvent exchange, polymeric gels may swell or deswell, depending on the solvent, by phenomena akin to osmosis.[51−53]

Table 1. General Material Properties of the PBO Aerogels[a]

name	linear shrinkage[b] (%)	bulk density, ρ_b (g cm^{-3})	skeletal density, ρ_s[c] (g cm^{-3})	porosity, Π[d] (% v/v)
PBO-7	38.88	0.25	1.31	80.92
PBO-10	40.30	0.37	1.30	71.54
PBO-12	38.88	0.46	1.32	65.15

[a]Average of five samples otherwise mentioned. [b]Shrinkage = 100 × (mold diameter − sample diameter)/(mold diameter). [c]Average of 50 measurements. [d]Porosity = 100 × $[(\rho_s - \rho_b)/\rho_s]$.

In the case of PBO wet gels no shrinkage was observed during solvent exchange from the gelation solvent (DMF) to the drying solvent (pentane). The shrinkage during ambient-pressure drying was also negligibly small (2%). Therefore, consistent with the definition of aerogels,[54−56] our dry PBO monoliths are termed aerogels. Finally, the major part of the total shrinkage (38%) occurred during the curing process (at 200 °C in air), which is well understood to cause oxidative ring-fusion aromatization along the polymeric backbone.[39] That process decreases the degrees of freedom along the polymeric chain and brings aromatic rings closer together, inducing molecular compaction and macroscopic shrinkage akin to what is observed in all materials classified as carbon aerogels. Bulk densities (ρ_b) of the aerogel samples were monotonically increasing with the increase of monomer concentration. However, skeletal densities (ρ_s) were constant and invariant of monomer concentration. For direct comparison, the density of the ambient-dried PBO samples of the present work was compared with the reported supercritically dried samples. The bulk densities obtained from the ambient-dried PBO-10 and PBO-12 samples were either equal to or less than their similar previously reported supercritical dried samples (see Table S2 in the Supporting Information). The bulk density of the ambient-dried PBO-7 was also only about 10% higher than its supercritical dried counterpart, which proves the effectiveness of our ambient-pressure drying approach and justifies referring to PBO-*xx* as aerogels rather than xerogels.

The porous structure of the PBO aerogels was studied through N_2-sorption measurements (see Figure 4) at all three densities, and representative results are summarized in Table 2. No signs of microporosity can be found in N_2-soprtion isotherms, which points to the fact that the PBO aerogels are partly mesoporous and mainly macroporous materials. It is worth mentioning that the hysteresis loops become wider and reach shorter saturation plateaus at higher densities, which means that the mesoporous portion of the materials at higher densities is larger than that at lower densities. Quantitatively, the open pore volume and the average pore diameter of the aerogels were also calculated (Table 2). As the density increases, the open pore volume (V_{Total}), which accounts for the entire open porosity of the samples, decreases. The pore sizes calculated via the $4V/\sigma$ are widely different with $V = V_{Total}$ and the V from the single-point adsorption method. However, the pore sizes calculated from BJH method are converging, especially at the highest density samples.

2.3.2. Structural Properties. SEM images of the PBO aerogel samples are shown in Figure 5. PBO-*xx* aerogel samples consisted of ∼60−100 nm particles in agreement with N_2-sorption based calculations (Table 2). This cross-agreement is inherently remarkable. The aerogel microstructure formation mechanism is the result of a random secondary

DOI: 10.1021/acsapm.9b00408
ACS Appl. Polym. Mater. 2019, 1, 2322−2333

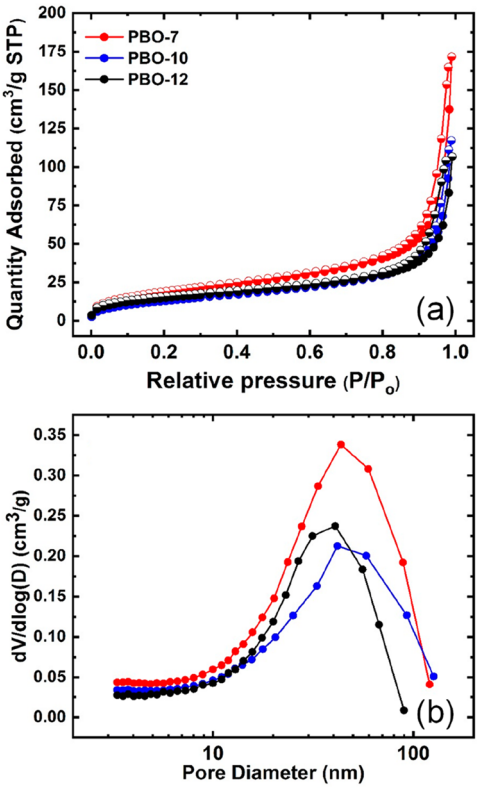

Figure 4. N_2-sorption measurements of the PBO aerogels: (a) isotherm and (b) BJH plots.

particle aggregation mechanism (i.e., random cluster-like models) which remained essentially the same at different densities. Water contact angles on smooth and sanded PBO aerogel surfaces were also measured at room temperature (see Figure 5). Practically, all aerogel samples were superhydrophobic with contact angles reaching 159.0 ± 1.6°. Upon submerging the PBO samples in water, the silver mirror effect can be observed on these superhydrophobic surfaces due to the light reflection from the trapped water layer at both ends of the samples. It should be mentioned that these effects cannot be seen on the circumferential surface of the sample as a result of the surface remodifications by molding. Movie S1 shows the silver mirror effect for PBO-10 in water. This kind of hydrophobicity (i.e., with contact angles above 120°) is attributed to texture[43] and renders PBO-*xx* aerogels suitable as an alternative low-cost, multifunctional hydrophobic coating or for environmental remediation applications as an oil-removing material.[44]

2.4. Thermomechanical Characterization. *2.4.1. Quasi-Static Uniaxial and Shear Properties at Room Temperature.* The fundamental mechanical properties of the aerogels at low strain rate (i.e., 0.001 s^{-1}) were studied at room temperature (Figure 6). The typical stress−strain curves of the PBO samples in compression are depicted in Figure 6a. The compression behavior of the PBO aerogels follow three stages of elastic deformation, compaction, and densification. No buckling was observed during the compression experiments. It can be noted that the ratio of the collapse strain (i.e., strain level at the failure) to the sample's porosity is about 0.8 and remains constant at different densities. Therefore, the overall compressibility of the samples can be controlled by the sample's porosity. Furthermore, the density dependencies of the Young's modulus and the yield strength (i.e., stress at 0.2% offset) of the PBO samples were studied (Figure 6b). Both the Young's moduli and the yield strengths of the PBO samples are clearly higher than those of polyimide[31] and polyamide (Kevlar-like) aerogels[32] as well as classical X-silica and X-vanadia (obtained from Table 3 in ref 21) aerogels over the entire density range of this study. The scaling relationship with respect to density (i.e., ρ^m) leads to the exponents of 3.2 and 3.6 for the Young's modulus and the yield strength, respectively. The Poisson's ratios of the PBO aerogels were also measured by using a 3D Digital Image Correlation (DIC) technique concurrent with the compression tests. The strain fields along the *X* and *Y* directions of the PBO-10 aerogel sample are demonstrated as an example in the Supporting Information (Figure S1). The PBO aerogels have low Poisson's ratios (0.23) even at higher densities (0.46 g/cm^3; the PBO-12 samples), which is an indication of only a small expansion during the compression process. The low Poisson's ratio observation is also in agreement with the porosity-controlled compressive behavior of the aerogels. Therefore, it can be concluded that after the elastic deformation, the primary plastic deformation is correlated to the self-contraction of the sample into its own pores followed by a brittle fragmentation at the rupture strain (the inset in Figure 6a shows a typical PBO sample before and after the compression test). Table 3 summarizes the quasi-static compressive properties of the PBO samples at room temperature.

To examine the material durability, different cyclic loading−unloading compression tests must be carried out. Following the existence of a scaling behavior for the PBO samples with respect to their densities, cyclic loading−unloading compression tests can be performed only at one density. Therefore, the number of required experiments can be dramatically reduced. In this way, the stability and resilient property of the aerogels under cyclic loadings were studied by using the cyclic loading−unloading compression test at −20% strain level for PBO-10 as a benchmark sample (Figure 6c). At this strain level, a decent plastic deformation can be applied on the sample. The starting point at each cycle is the same and equal to the initial sample length for the entire 100 cycles. A transient behavior is

Table 2. General Porous Properties of the PBO Aerogels

		specific pore volume (cm^3 g^{-1})			average pore diameter (nm)		
name	BET surface area, σ (m^2 g^{-1})	V_{Total} [a]	$V_{1.7-300nm}$ [b]	$V_{>300nm}$ [c]	$4V/\sigma$ [d]	BJH method [e]	particle diameter, D [f] (nm)
PBO-7	68	3.00	0.25	2.75	177.33 [15.70]	43.49 [71.67]	67.40
PBO-10	49	1.95	0.17	1.77	159.37 [14.84]	41.81 [79.01]	94.92
PBO-12	54	1.36	0.15	1.21	101.58 [12.32]	40.77 [46.82]	84.90

[a] $V_{Total} = (1/\rho_b) - (1/\rho_s)$. [b] BJH desorption cumulative pore volume. [c] $V_{>300} = V_{Total} - (V_{1.7-300})$. [d] For the first number, *V* was V_{Total}; for the number in parentheses, *V* was calculated by the single-point adsorption method. [e] From the BJH plots, first numbers are peak maxima; numbers in parentheses are full widths at half-maxima. [f] $D = 6/\rho_s\sigma$.

DOI: 10.1021/acsapm.9b00408
ACS Appl. Polym. Mater. 2019, 1, 2322−2333

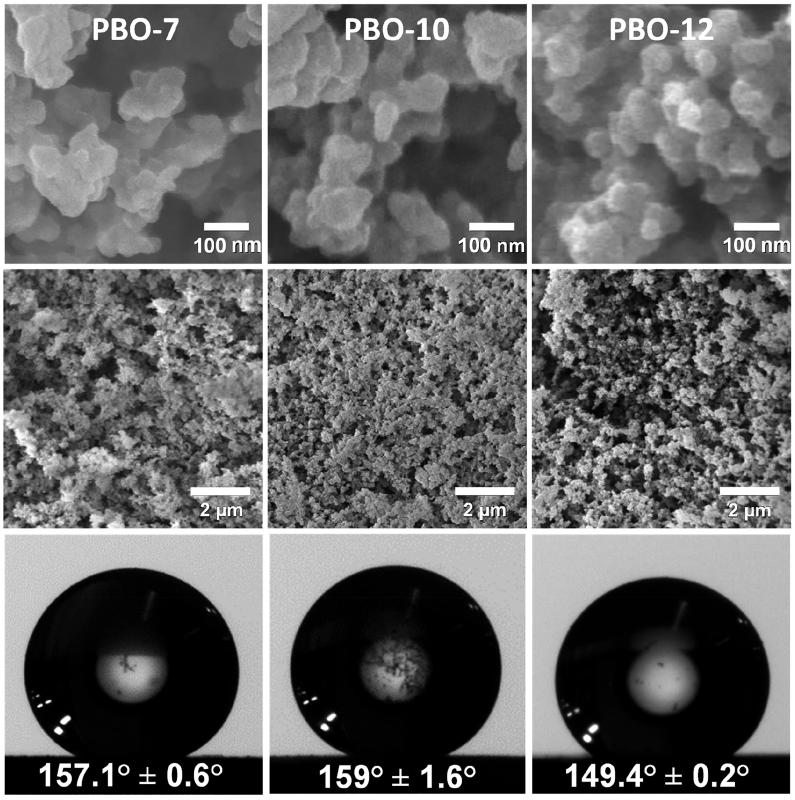

Figure 5. SEM micrographs at two magnifications of the PBO aerogels and the water drop (5 mL) average contact angles on the smooth and sanded PBO-*xx* aerogel surfaces, pointing to a superhydrophobic state.

observed in the cyclic stress−strain response of the PBO aerogel. The Young's modulus and the peak stress at −20% strain level as a function of the number of cycles are shown in Figure 6d. The general behavior of the peak stress is indicative of a relaxation mechanism, mainly due to possible crack initiations in each cycle (only ∼15% drop during 100 cycles). However, the apparent Young's modulus (i.e., modulus in Figure 6d) as a function of the number of loading cycles shows a drop during the first ten cycles essentially as a result of microstructural buckling, adhesion and friction between polymeric branches, and crack formation due to the large initial plastic deformations. Afterward, the apparent Young's modulus starts to gradually increase continuously to the last cycle. This phenomenon is called "plastic (or mechanical) preconditioning" which is related to the removal or a significant reduction in the polymer intrinsic postyield softening after applying cyclic deformations.[45] The modulus enhancement is simultaneous with the gradual decrease in the permanent plastic strain after the unloading part of each cycle which is ultimately ended to a complete viscoelastic loading−unloading cycle without any plastic deformation at 100th cycle (see Figure 6c).

In the next compression test, the PBO-12 samples were considered as the benchmark and were compressed quasi-statically at five-stepped cycles at different strain levels of −5, −10, −20, −30, and −45%, in sequence. In this experiment, in contrast with the previous one, the starting point at each cycle is the end of the unloading part of the previous cycle. Figure 6e shows the cyclic stress−strain curve of a PBO-12 sample containing a nonlinear recovery at each unloading curve. This nonlinear unloading path is due to the material's inherent viscosity, which causes the displacement to lag behind the load. All loading curves rise back to the maximum stress point of their own previous cycle, indicating of the presence of a strong memory effect in the PBO aerogels. The origin of this memory effect would be the programmed plastic stress state in the polymer chains during the previous loading cycle that can be reached after unloading and reloading steps. At each cycle, the reloading part does not follow the unloading part, resulting in the formation of a hysteresis loop. The formation of hysteresis loops is related to the mechanical energy absorption and later dissipation as heat as a result of internal friction within the material. Furthermore, the torsional properties of the PBO-12 samples were studied via a quasi-static pure torsion test on intact and preloaded samples. Figure 6f shows the shear stress−strain curves of the PBO-12 samples. Despite the compressional ductility in the PBO aerogels, they are brittle in torsion. The typical PBO sample before and after the torsion test is shown in the inset of Figure 6f. For homogeneous isotropic materials, the shear modulus (G) can be calculated via the equation[46]

$$G = \frac{E}{2(1+\nu)} \tag{1}$$

where E is the Young's modulus and υ is the Poisson's ratio. Using eq 1 and the experimental data obtained from Table 3 for the PBO-12 sample, we estimated the shear modulus to be 90.4 MPa while the experimental shear modulus (i.e., ∼177 MPa) is almost 2 times stiffer, which confirms the existence of a *strong anisotropy* in the PBO aerogels. The results for the preloaded sample also show no drop in the shear modulus even after 4000 preloading cycles on the PBO aerogels which

DOI: 10.1021/acsapm.9b00408
ACS Appl. Polym. Mater. 2019, 1, 2322−2333

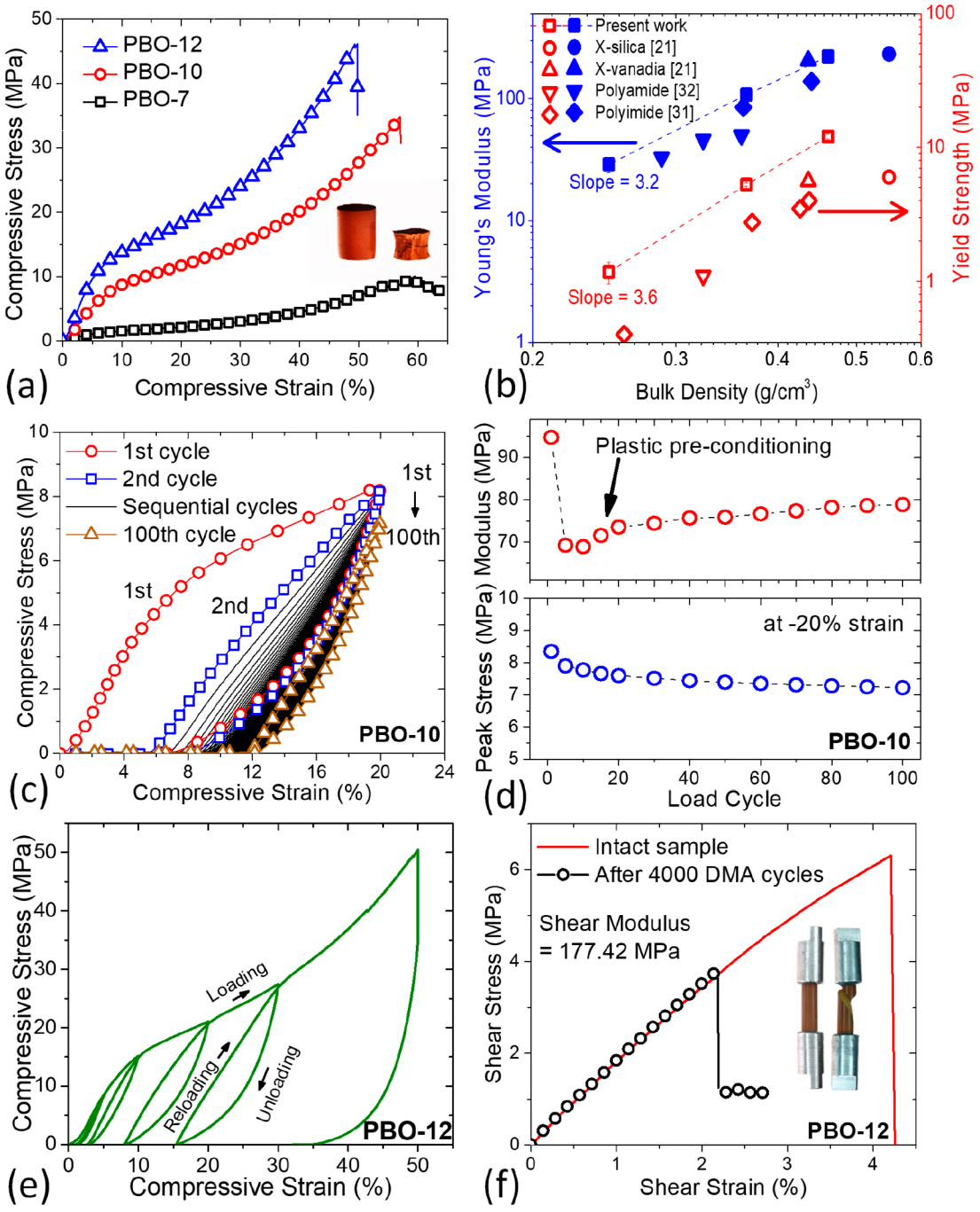

Figure 6. (a) Typical quasi-static uniaxial compression stress−strain responses of the PBO aerogels at different bulk densities. (b) Power-law relationships of the Young's modulus and the yield strength with bulk density of the PBO aerogels along with those values for X-silica, X-vanadia, polyimide, and polyamide (Kevlar-like) aerogels at the same density range. (c) Cyclic quasi-static load−unload compression testing at −20% strain of PBO-10 for 100 cycles. (d) Apparent Young's modulus (top) and peak stress (bottom) values of the PBO-10 at different cycles. (e) Sequential cyclic load−unload−reload compression testing of the PBO-12 sample. (f) Quasi-static pure torsion testing of intact and preloaded PBO-12 samples. All experiments have been performed at room temperature. Insets in (a) and (f) are the typical PBO samples before and after quasi-static compression and pure torsion tests, respectively.

confirms the strong mechanical durability for these PBO aerogels.

2.4.2. Quasi-Static Compressive Properties at Elevated Temperatures. To assess the mechanical performance of the aerogels at elevated temperatures, systematic quasi-static compression experiments at different densities were carried out. The samples were placed in a heat chamber at the target temperature for at least 45 min before starting the test. The typical stress−strain curves of PBO-12 at different temperatures are shown in the Supporting Information (see Figure S2). The fundamental mechanical properties of the PBO samples as a function of temperature are shown in Figure 7a−d. The Young's modulus of the aerogels at different temperatures, shown in Figure 7a, represents a gradual softening at similar rate for all densities. At the highest temperature (i.e., 250 °C), in comparison with room

DOI: 10.1021/acsapm.9b00408
ACS Appl. Polym. Mater. 2019, 1, 2322−2333

Table 3. Quasi-Static Compressive Properties of the PBO Aerogels at Room Temperature[a]

name	Young's modulus (MPa)	Poisson's ratio[b]	yield stress[c] (MPa)	ultimate strain[d]
PBO-7	28.90 ± 4.21	0.14	1.17	55.74
PBO-10	107.88 ± 2.46	0.19	5.27	50.06
PBO-12	222.38 ± 6.63	0.23	12.04	48.00

[a]Average of three measurements. [b]Average Poisson's ratio of initial 5% compressive strains. [c]Measured via the 0.2% offset method. [d]Strain at the first drop of stress–strain curve.

temperature, the Young's modulus was decreased by ~55% for PBO-7 and PBO-10 while this drop is ~45% for PBO-12. A higher density of cross-linked networks at PBO-12 in comparison with the other two lower density samples could be related to the lower drop in the Young's modulus over a similar temperature change, although it should be noted that PBO-12 is still a low-density sample (i.e., 0.46 g/cm^3). On the other hand, the compressive strength (i.e., 0.2% offset yield point) has an initial hardening at low temperatures (Figure 7b) unlike most other glassy polymers. The increase in the strength with the rise of temperature to 50 °C might be partly related to the expansion of the trapped air molecules and a low-energy conformational adjustment process in the aerogel samples which needs to be studied further. However, pragmatically, high-temperature structural applications can definitely realize leverage from this enhancement as the compressive strength at 150 °C at all densities is equal to their room-temperature values. Also, the compressibility of the aerogels is improved from ~50% to ~60% as a result of temperature increase to 200 °C (Figure 7c). All these different behaviors indicate that PBO aerogels are extremely thermally resilient at elevated temperatures. In the last part of those experiments, the effect of temperature soaking-time on the mechanical behavior of the PBO aerogels was examined. Two sets of experiments each repeated three times (only PBO-10 was tested) were performed in the heat chamber at the target temperature (i.e., 200 °C) for 45 min and 24 h. The average compressive stress–strain curves of the two PBO-10 experiments are shown in Figure 7d. Clearly, the longer soaking time caused an overall hardening in both the modulus and the strength of the material, probably due to further conformational adjustments, which is very attractive for practical engineering applications where the material will stay at high service temperatures for a long time. Moreover, the dynamic temperature distribution of the PBO aerogels at the lowest density on a heat stage was monitored by using an infrared camera (Figure 7e). The temperature gradient from the heat stage through the other end of the aerogel sample was continuously growing for the initial 10 s and maintained relatively unchanged after 1 min. The heat stage was at 100 °C with a room temperature at 17 °C. The opposite end of the PBO sample with only 23 mm length was at 17 °C for the entire time, which indicates the strong thermal insulation properties of these aerogels. This interesting behavior led us to measure the thermal conductivities of the PBO aerogels at all densities. The results are listed in Table 4. The aerogels showed a thermal conductivity of 0.097 W/(m K) at the lowest density up to 0.13 W/(m K) at the highest density. Compared to silica aerogel, the thermal conductivities are higher, but still the PBO aerogels can be considered as thermally insulating materials. In comparison with phenolic foams (conventional thermal insulators)[49] of

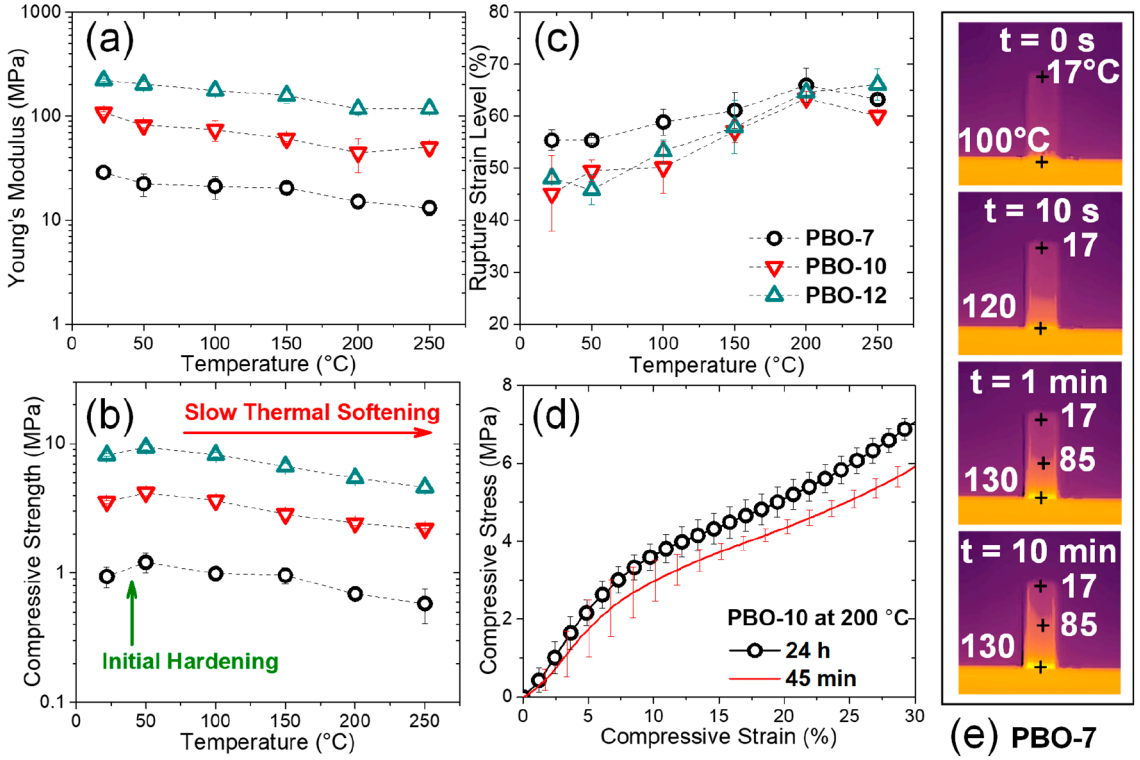

Figure 7. Quasi-static compressive properties of PBO aerogels at elevated temperatures: (a) Young's modulus, (b) compressive strength, and (c) rupture strain level. (d) Effect of thermal soaking time on the compressive stress–strain behavior of PBO-10 sample. (e) Infrared images of PBO-7 sample (23 mm length and 7.6 mm diameter) on a heating stage for 10 min.

DOI: 10.1021/acsapm.9b00408
ACS Appl. Polym. Mater. 2019, 1, 2322–2333

Table 4. Heat Capacity, Thermal Diffusivity, and Thermal Conductivity of the PBO Aerogels at Room Temperature

name	bulk density, ρ_b (g cm^{-3})	heat capacity, c_p (J g^{-1} K^{-1})	thermal diffusivity, R (mm^2 s^{-1})	thermal conductivity, λ (W m^{-1} K^{-1})
PBO-7	0.262 ± 0.006	1.274 ± 0.335	0.292 ± 0.028	0.097 ± 0.033
PBO-10	0.379 ± 0.016	0.932 ± 0.272	0.353 ± 0.111	0.125 ± 0.037
PBO-12	0.483 ± 0.016	1.229 ± 0.338	0.219 ± 0.045	0.130 ± 0.044

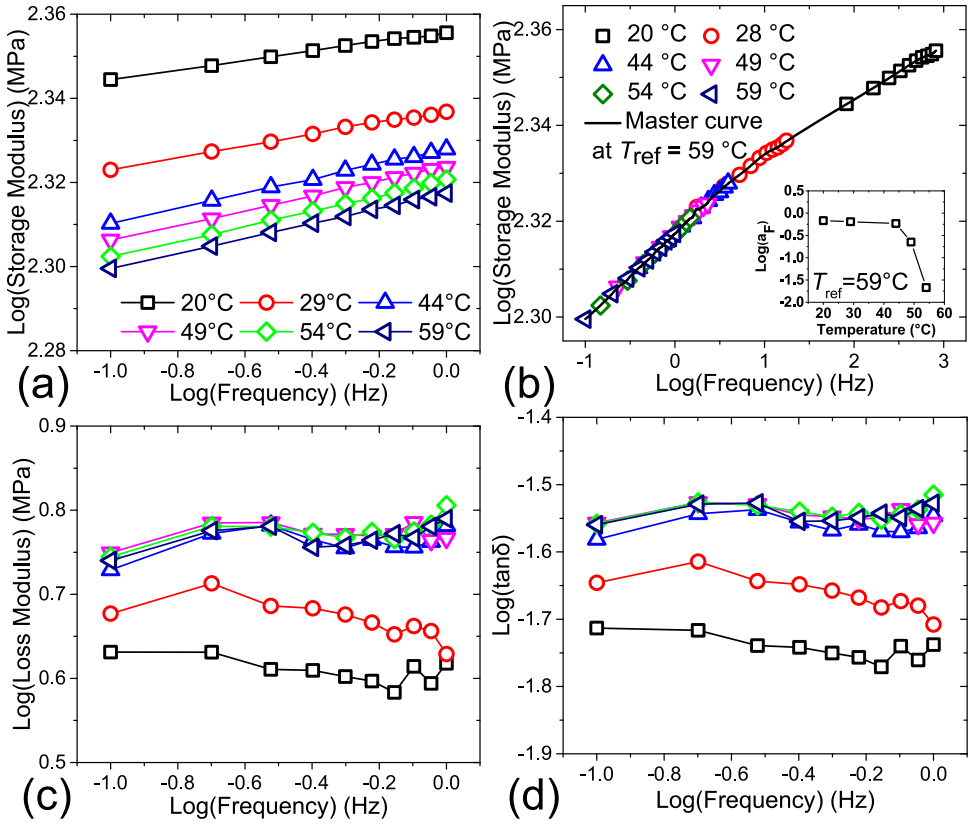

Figure 8. Shear viscoelastic properties of PBO-12 sample as a function of frequencies at different temperature: (a) storage modulus, (b) master curve for storage modulus and the storage shift factor at different temperature in the inset, (c) loss modulus, and (d) tan δ.

similar density, the thermal conductivities of PBO aerogels are lower; however, compared to those of the phenolic aerogels including resorcinol–formaldehyde-derived aerogels,[3] the PBO thermal conductivities are higher.[50] The flammability of the aerogels was also studied under a direct external flame. The aerogels were self-extinguishing, and their structural integrity was retained in both carbonized and uncarbonized regions (see Movie S2). To study the material degradation with respect to heat in the PBO aerogel samples, thermogravimetric analyses (TGA) were performed, and the results are shown in Figure S3. The TGA results show that all samples are equally resistant to heat and start to lose mass at about 330 °C. Up to 700 °C, only 50% mass loss, at maximum, was observed for the aerogels. These results considered together indicate that the PBO aerogels could serve the dual function of a robust fire-proof thermal insulator in a broad range of engineering applications.

2.4.3. High-Torque Dynamic Mechanical Analysis in Shear at Elevated Temperatures. Dynamic mechanical analysis (DMA) has been used extensively by material scientists to obtain the viscoelastic properties of polymeric materials. However, in most cases, the material is underloaded in their elastic region. In other words, the applied load is usually very small, and therefore the true viscoelastic response of the material might not be observed. On the other hand, while special attention must be made to carry out the experiments in the elastic region of the material, the DMA experiment can be operated at higher load/torque amplitudes by using a high-force/torque DMA setup. Here, the viscoelastic properties of the PBO aerogel in shear mode were measured by using an Instron ElectroPuls E10000 load frame (for more details refer to the Experimental Section). Under the cyclic rotational control mode, the PBO-12 sample was tested at 1% shear strain offset with 0.1% oscillatory shear strain amplitude at different temperatures and rotational frequencies. Under those conditions, the sample experienced a 3° rotational angle offset and a 0.5° oscillatory rotational angle amplitude, which is considered a large oscillatory amplitude for the proposed viscoelastic characterization. Figure 8 shows the shear viscoelastic properties of PBO-12 at different rotational frequencies and elevated temperatures. To reach equilibrium conditions, samples were held at least for 45 min at each target temperature. Then, the steady-state response (torque) to the harmonic excitation (rotational angle) was measured. The storage modulus is shown in Figure 8a. In the log–log plane, the storage modulus as a function of frequency at each temperature showed a straight line. The storage was reduced with increasing temperature. Even though applied temperatures were well below the glass transition regime, the dynamic modulus was very sensitive to the temperature. The

DOI: 10.1021/acsapm.9b00408
ACS Appl. Polym. Mater. 2019, 1, 2322–2333

equivalence concept between frequency and temperature was then used to construct a viscoelastic master curve for the storage modulus following the frequency−temperature superposition principle.[47] The storage master curve for PBO-12 at the reference temperature of 59 °C is shown in Figure 8b. The associated shift factor plot is also shown in the inset of Figure 8b, namely, the logarithmic shift factor, $\log(a_F)$. Although the storage moduli were only measured up to 1 Hz, the obtained master curve can be utilized to represent the PBO aerogel behavior over 3 decades of frequency (i.e., up to 1000 Hz). Loss moduli were typically lower than the corresponding storage values over the entire frequency and temperature range (Figure 8c). At 44 °C and above, the loss moduli were not changing. A similar trend can be seen for the behavior of tan δ, which is defined as the ratio of loss over storage moduli (Figure 8d). It is worth mentioning that the storage modulus of the aerogels tripled at highest frequencies with respect to the quasi-static loading condition, which shows a high-frequency dependence.[48]

The isofrequency shear storage and loss moduli of the PBO-12 aerogels at 1 Hz as a function of temperature are shown in Figure 9. The storage (loss) modulus at 60 °C was about 10%

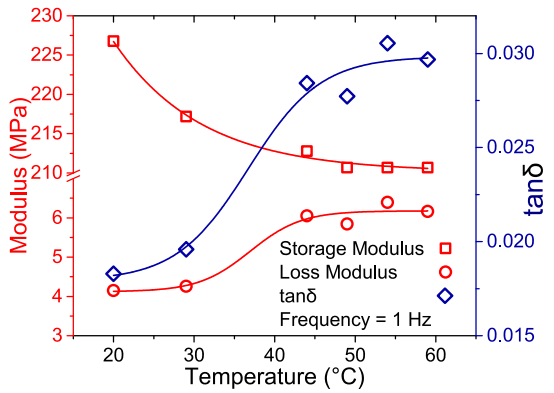

Figure 9. Isofrequency shear complex modulus and tan δ of PBO-12 as a function of temperature at reference frequency of 1 Hz.

lower (higher) than that at 20 °C, indicative of a robust dynamic behavior for the aerogels at elevated temperatures. In future work, the frequency-dependent storage master curve can be correlated to the shear creep master curve through the interconversion of linear viscoelastic properties.

3. CONCLUSION

PBO aerogels were prepared at room temperature and dried under ambient pressure at bulk densities even lower than their supercritical dried counterparts of similar monomer concentration. Curing in air stabilized the structure and rendered the resulting materials suitable for high-temperature applications. PBO aerogels showed a highly promising combination of excellent mechanical properties with superhydrophobicity, low thermal conduction, and fire resistance. In particular, the high Young's modulus and mechanical strength of the PBO aerogels in comparison with other high-performance polymeric and polymer cross-linked aerogels at all densities generate new design options for high-performance structural applications. Their robust thermomechanical properties with low thermal conductivity and fire retardancy render these aerogels excellent candidates for commercial thermal protection applications.

4. EXPERIMENTAL SECTION

4.1. Materials. Anhydrous acetone, anhydrous acetonitrile, anhydrous pentane, aniline, chloroform, hydrochloric acid, *N*,*N*-dimethylformamide (DMF), and sodium hydroxide were obtained from Fisher Scientific (Hampton, NH). Bisphenol A (BPA) and paraformaldehyde were supplied by Frontier Scientific (Logan, UT). Five milliliter plastic vials were used as molds. All purchased materials were used without further processing except for aniline, which was extra-distilled.

4.2. Synthesis of BO Monomer. In the synthesis, 22.82 g of BPA, 12.01 g of paraformaldehyde, and 18.23 mL of distilled aniline were combined in a round-bottom flask. The mixture was stirred continuously for 1 h in an oil bath that was maintained at 80 °C. The mixture turned to a light yellow solid. Then chloroform was added to the flask at 55 °C until the solid was fully dissolved. Next, the solution was extracted three times with a freshly prepared 3 M sodium hydroxide solution and three times with deionized water. The solution was dried over anhydrous sodium sulfate and filtered to remove water. The chloroform was then removed by heating on a hot plate at about 55 °C until the resulting mixture became a clear, viscous yellow liquid. The liquid was vacuum-dried at room temperature for 24 h, after which it became a fluffy, pale yellow, crystalline powder.

4.3. Preparation of PBO Aerogels. In a typical synthesis, BO monomer and 12.1 N HCl catalyst were separately dissolved in DMF (exact values are listed in Table S1). The two solutions were combined and stirred at room temperature for 10 min. The resulting sols were poured into molds and were allowed to gel. Wet gels were aged in their molds for 24 h at room temperature. Afterward, wet gels were removed from the molds and washed successively twice with DMF, acetone, acetonitrile, and pentane, allowing a 12 h stay in each bath. Pentane-filled wet gels were allowed to dry at room temperature and pressure for 24 h. The resulting aerogels were then step-cured in an regular oven in air at 160 °C for 30 min, at 180 °C for 30 min, and finally at 200 °C for 24 h. The final materials are termed PBO-*xx*, where *xx* stands for the weight percent of the monomer concentration in the sol.

4.4. Chemical Characterization. Solid-state CPMAS ^{13}C NMR spectra were obtained with powdered samples on a Bruker Avance III 400 MHz spectrometer with a carbon frequency of 100 MHz using a 7 mm Bruker MAS probe at a magic angle spinning rate of 5 kHz with the CPMAS pulse sequence. The magic angle spinning (MAS) pulse sequence was applied by using a series of four properly timed 180° pulses on the carbon channel at different points of a cycle before acquisition of the FID, after an initial excitation with a 90° pulse on the proton channel. The 90° excitation pulse on the proton and the 180° excitation pulse on carbon were set to 4.2 and 10 μs, respectively. A contact time of 3 ms was used for cross-polarization.

Infrared (IR) spectra were obtained using a Nicolet-FTIR Model 750 spectrometer by mixing the sample with KBr and then compressing it to pellets.

4.5. Physical Characterization. Bulk densities (ρ_b) were determined from the weight and the physical dimensions of the samples. Skeletal densities (ρ_s) were determined with helium pycnometry using a Micromeritics AccuPyc II 1340 instrument. Porosities (Π) as a percent of empty space were determined from the ρ_b and ρ_s values via $\Pi = 100 \times [(\rho_s - \rho_b)/\rho_s]$. Surface area and pore size distributions were determined with N_2-sorption porosimetry using a Micromeritics ASAP 2020 surface area and porosity analyzer equipped with a low-pressure transducer (0.1 Torr) for micropore analysis. Samples for porosimetry and skeletal density determination were degassed for 24 h, at 80 °C, under a vacuum, before analysis. Average pore diameters were determined with the $4V/\sigma$ method, where V is the pore volume per gram of sample and σ is the surface area determined by the Brunauer−Emmett−Teller (BET) method. V either can be taken as the single highest volume of N_2 adsorbed along the adsorption isotherm or can be calculated from the relationship $V = V_{Total} = (1/\rho_b) - (1/\rho_s)$. Materials lack macroporosity when the two average pore diameters calculated with the two different V values coincide. Scanning electron microscopy (SEM) was conducted with

DOI: 10.1021/acsapm.9b00408
ACS Appl. Polym. Mater. 2019, 1, 2322−2333

Au/Pd (60/40) coated samples on a Hitachi Model S-4700 field emission microscope. The sample was placed on the stub with a C-dot. Thin sticky Cu strips were cut and placed on the edges and top of the sample leaving some space for the analysis. Water-contact angles were measured with a ramé-hart Model 250 standard goniometer equipped with a high-resolution camera, using the static sessile drop method, in which a 5 μL droplet of water is placed on the sample surface followed by imaging. The samples were prepared by cutting disks with a knife; surfaces were smoothened with sandpaper (3M Abrasives, 320 grit, part no. 32541) and were cleaned with a stream of dry N_2 at high pressure. Contact angle data were collected using three separate samples for each run (formulation) immediately upon placement of the water droplets on the samples. Contact angles were determined with the DROPimage Advanced v2.4 software. A total of 10 measurements were taken by the computer in rapid succession. Results were reported as averages over the three samples (30 measurements) for each formulation.[43] For thermal insulation studies, the sample was placed on the hot plate set at 100 °C, and then the dynamic temperature distribution in the sample was observed by using a FLIR infrared camera (FLIR Systems, Inc., Model: FLIR ONE PRO). TGA analysis was performed on a TGA/DSC 1 STARe System (Mettler Toledo AG Analytical, Switzerland) with a temperature range of 50−700 °C and a ramp rate of 10 °C min^{-1} under an N_2 atmosphere. The total thermal conductivities of all samples were calculated at 23 °C via $\lambda_{Total} = R \times c_p \times \rho_b$, as has been described recently.[43] The thermal diffusivity, R, of each sample was determined at room temperature and atmospheric pressure with a Netzsch NanoFlash Model LFA 447 flash diffusivity instrument using disk samples ~1 cm in diameter and 2−3 mm thick. Specific heat capacities, c_p, at 23 °C were measured with powders of the samples (5−10 mg) by using a TA Instruments differential scanning calorimeter Model Q2000 calibrated against a sapphire standard and run from 0 to 30 °C at 1.0 °C min^{-1} in the modulated T4P mode. The modulation amplitude was set at 0.133 °C and the modulation period at 100 s. PBO aerogel samples and two standards (rutile and corundum) were outgassed for 24 h, at 80 °C, under vacuum, before heat capacity measurements. First, the heat capacities of rutile and corundum were measured three times each just before running the PBO samples. These experimental heat capacity values were compared with literature values and were used to calculate a calibration factor (= 0.969). Then, we measured the heat capacities of the three PBO aerogels under the same conditions using three samples from each formulation. The heat capacity values of each sample were multiplied by the calibration factor.

4.6. Mechanical Characterization. Quasi-static compression tests were performed on an Instron mechanical testing system (Instron Inc., Model 5969, Norwood, MA) with 1 kN load cell (with an accuracy of 0.5% of the reading). The compression strain rate was set to 0.001 s^{-1}. Cylindrical-shaped samples with 7.6 mm diameter and heights ranging from 8 to 11 mm were cut from a larger PBO aerogel cylindrical sample. Three samples at each density were tested. To measure the Poisson ratios of the aerogels at room temperature, a random speckle pattern was generated on the surface under observation of the compression test sample using a quick drying white ink. The three-dimensional DIC technique, a noncontact full-field deformation measurement method, was used to measure the surface deformations using commercially available 3D SpeckleTrack software (Framingham, MA). Two CCD cameras (BASLER acA3800-14um, Germany) and their lenses (Kowa F1.8 mm, Japan) are used to acquire the left and right images (3840 pixels × 2748 pixels) of the test sample after several calibrations. For high temperature mechanical measurements, an Instron environmental chamber (Instron Inc., Model 5969, Norwood, MA) was used. The sample was soaked at the target temperature for at least 45 min before the measurement. Three measurements have been made at each temperature for each density. Quasi-static shear tests were performed by using an Instron Electropuls E10000 load frame (Instron Inc., Norwood, MA) with a 1 kN load cell and a 25 N m torque cell. Cylindrical samples with a diameter of 7.6 mm and height of 23 mm were glued to the torsion grips. Special attention has been made to ensure that the contact shear strength is being higher than the maximum shear strength of the sample. The samples were glued to the grips using a two-part epoxy glue (J-B Weld Co., Sulfur Springs, TX) with a nominal strength of 3960 psi. The torsion rate was set to 1°/min for quasi-static pure torsion tests. No significant normal stress was observed during the torsion tests. It is worth mentioning that the signal/noise ratio of the measurements was dramatically improved when all transducers' signals were balanced after the frame is on full power. DMA measurements in torsion were also performed on a sample with a similar configuration as the pure torsion tests using the same Instron Electropuls E10000 load frame. The sample was soaked at the target temperature for at least 45 min before the measurement. One sample is used for all measurements. In a rotational control mode, the steady-state response (torque) to the harmonic excitation (rotational angle) was measured. For each frequency, 50 cycles were considered. The rotational angle was set to a 3° offset (1% shear strain) and oscillating rotational amplitude of 0.5° (0.1% shear strain). A similar Instron environmental chamber (Instron Inc., Model 5969, Norwood, MA) was used for high-temperature measurements with at least 45 min thermal soaking.

■ ASSOCIATED CONTENT

Supporting Information

The Supporting Information is available free of charge on the ACS Publications website at DOI: 10.1021/acsapm.9b00408.

Synthesis amounts, gelation time, supercritical dried density; bulk density comparison between supercritical and ambient dried PBO aerogels of similar monomer concentrations; DIC strain field images; stress−strain curve of PBO-12 at different temperatures; thermogravimetric analysis of PBO aerogels (PDF)

Silver mirror effect on PBO-10 in water (MP4)

Flammability test on PBO aerogels (MP4)

■ AUTHOR INFORMATION

Corresponding Authors

*E-mail hongbing.lu@utdallas.edu; phone 972-883-4647 (H.L.).

*E-mail leventis@mst.edu; phone 573-341-4391 (N.L.).

ORCID

Sadeq Malakooti: 0000-0002-7648-5740

Nicholas Leventis: 0000-0002-7575-9498

Hongbing Lu: 0000-0003-4268-7245

Author Contributions

S.M. and G.Q. contributed equally to this work.

Notes

The authors declare no competing financial interest.

G.Q.: Visitor scholar from School of Materials Science and Engineering, Shijiazhuang Tiedao University, Shijiazhuang 050043, China.

N.T. and J.S.: High school summer researcher, St. Mark's School of Texas, Dallas, TX 75230.

■ ACKNOWLEDGMENTS

The support by AFOSR FA9550-14-1-0227, NSF CMMI-1661246, CMMI-1636306, and CMMI-1726435 and Nashi New Materials in China is acknowledged. N.L. and C.S.-L. thank the Army Research Office for financial support under W911NF-14-1-0369 and NSF under CMMI-1530603. G.Q. thanks Shijiazhuang Tiedao University for the financial support. We thank Dr. X. Hu and Dr. T. Ware for the FTIR measurements and Dr. B. Batchelor and Dr. W. Voit for the TGA measurements. The support from STEM Bridge summer

DOI: 10.1021/acsapm.9b00408
ACS Appl. Polym. Mater. 2019, 1, 2322−2333

camp for high school students via Chinese Association for Science and Technology (CAST) is acknowledged. H.L. is also grateful to the support by the Louis Beecherl Jr. Endowed Chair.

REFERENCES

(1) Bauer, J.; Meza, L. R.; Schaedler, T. A.; Schwaiger, R.; Zheng, X.; Valdevit, L. Nanolattices: An Emerging Class of Mechanical Metamaterials. *Adv. Mater.* **2017**, *29* (40), 1701850.
(2) Li, Q.; Chen, L.; Gadinski, M. R.; Zhang, S.; Zhang, G.; Li, H. U.; Iagodkine, E.; Haque, A.; Chen, L.-Q.; Jackson, T. N.; Wang, Q. Flexible High-Temperature Dielectric Materials from Polymer Nanocomposites. *Nature* **2015**, *523*, 576.
(3) Galinski, H.; Favraud, G.; Dong, H.; Gongora, J. S. T.; Favaro, G.; Döbeli, M.; Spolenak, R.; Fratalocchi, A.; Capasso, F. Scalable, Ultra-Resistant Structural Colors Based on Network Metamaterials. *Light: Sci. Appl.* **2017**, *6* (5), No. e16233.
(4) Yu, R.; Ching, K.-L.; Lin, Q.; Leung, S.-F.; Arcrossito, D.; Fan, Z. Strong Light Absorption of Self-Organized 3-D Nanospike Arrays for Photovoltaic Applications. *ACS Nano* **2011**, *5* (11), 9291−9298.
(5) *Sol-Gel Science: The Physics and Chemistry of Sol-Gel Processing*; Brinker, C. J., Scherer, G. W., Eds.; Academic Press: 1990.
(6) Pierre, A. C. History of Aerogels. In *Aerogels Handbook*; Springer: New York, 2011; pp 3−18.
(7) Malakooti, S.; Rostami, S.; Churu, H. G.; Luo, H.; Clark, J.; Casarez, F.; Rettenmaier, O.; Daryadel, S.; Minary-Jolandan, M.; Sotiriou-Leventis, C.; Leventis, N.; Lu, H. Scalable, Hydrophobic and Highly-Stretchable Poly(Isocyanurate-urethane) Aerogels. *RSC Adv.* **2018**, *8* (38), 21214−21223.
(8) Malakooti, S.; Churu, H. G.; Lee, A.; Rostami, S.; May, S. J.; Ghidei, S.; Wang, F.; Lu, Q.; Luo, H.; Xiang, N.; Sotiriou-Leventis, C.; Leventis, N.; Lu, H. Sound Transmission Loss Enhancement in an Inorganic-Organic Laminated Wall Panel Using Multifunctional Low-Density Nanoporous Polyurea Aerogels: Experiment and Modeling. *Adv. Eng. Mater.* **2018**, *20* (6), 1700937.
(9) Malakooti, S.; Churu, H. G.; Lee, A.; Xu, T.; Luo, H.; Xiang, N.; Sotiriou-Leventis, C.; Leventis, N.; Lu, H. Sound Insulation Properties in Low-Density, Mechanically Strong and Ductile Nanoporous Polyurea Aerogels. *J. Non-Cryst. Solids* **2017**, *476*, 36−45.
(10) Smirnova, I.; Gurikov, P. Aerogels in Chemical Engineering: Strategies Toward Tailor-Made Aerogels. *Annu. Rev. Chem. Biomol. Eng.* **2017**, *8* (1), 307−334.
(11) Lu, H.; Xiang, N.; Leventis, N.; Sotiriou-Leventis, C. Acoustic Attenuators Based on Porous Nanostructured Materials. US9068346B1, October 21, 2013.
(12) Toivonen, M. S.; Kaskela, A.; Rojas, O. J.; Kauppinen, E. I.; Ikkala, O. Ambient-Dried Cellulose Nanofibril Aerogel Membranes with High Tensile Strength and Their Use for Aerosol Collection and Templates for Transparent, Flexible Devices. *Adv. Funct. Mater.* **2015**, *25* (42), 6618−6626.
(13) Leventis, N.; Sotiriou-Leventis, C.; Zhang, G.; Rawashdeh, A.-M. M. Nanoengineering Strong Silica Aerogels. *Nano Lett.* **2002**, *2* (9), 957−960.
(14) Katti, A.; Shimpi, N.; Roy, S.; Lu, H.; Fabrizio, E. F.; Dass, A.; Capadona, L. A.; Leventis, N. Chemical, Physical, and Mechanical Characterization of Isocyanate Cross-Linked Amine-Modified Silica Aerogels. *Chem. Mater.* **2006**, *18* (2), 285−296.
(15) Mulik, S.; Sotiriou-Leventis, C.; Churu, G.; Lu, H.; Leventis, N. Cross-Linking 3D Assemblies of Nanoparticles into Mechanically Strong Aerogels by Surface-Initiated Free-Radical Polymerization. *Chem. Mater.* **2008**, *20* (15), 5035−5046.
(16) Leventis, N.; Sotiriou-Leventis, C.; Mulik, S.; Dass, A.; Schnobrich, J.; Hobbs, A.; Fabrizio, E. F.; Luo, H.; Churu, G.; Zhang, Y.; Lu, H. Polymer Nanoencapsulated Mesoporous Vanadia with Unusual Ductility at Cryogenic Temperatures. *J. Mater. Chem.* **2008**, *18* (21), 2475.
(17) Luo, H.; Churu, G.; Fabrizio, E. F.; Schnobrich, J.; Hobbs, A.; Dass, A.; Mulik, S.; Zhang, Y.; Grady, B. P.; Capecelatro, A.; Sotiriou-Leventis, C.; Lu, H.; Leventis, N. Synthesis and Characterization of the Physical, Chemical and Mechanical Properties of Isocyanate-Crosslinked Vanadia Aerogels. *J. Sol-Gel Sci. Technol.* **2008**, *48* (1−2), 113−134.
(18) Mohite, D. P.; Larimore, Z. J.; Lu, H.; Mang, J. T.; Sotiriou-Leventis, C.; Leventis, N. Monolithic Hierarchical Fractal Assemblies of Silica Nanoparticles Cross-Linked with Polynorbornene via ROMP: A Structure-Property Correlation from Molecular to Bulk through Nano. *Chem. Mater.* **2012**, *24* (17), 3434−3448.
(19) Kim, C. H. J.; Zhao, D.; Lee, G.; Liu, J. Strong, Machinable Carbon Aerogels for High Performance Supercapacitors. *Adv. Funct. Mater.* **2016**, *26* (27), 4976−4983.
(20) Rewatkar, P. M.; Taghvaee, T.; Saeed, A. M.; Donthula, S.; Mandal, C.; Chandrasekaran, N.; Leventis, T.; Shruthi, T. K.; Sotiriou-Leventis, C.; Leventis, N. Sturdy, Monolithic SiC and Si_3N_4 Aerogels from Compressed Polymer-Cross-Linked Silica Xerogel Powders. *Chem. Mater.* **2018**, *30* (5), 1635−1647.
(21) Leventis, N.; Sotiriou-Leventis, C.; Chandrasekaran, N.; Mulik, S.; Larimore, Z. J.; Lu, H.; Churu, G.; Mang, J. T. Multifunctional Polyurea Aerogels from Isocyanates and Water. A Structure-Property Case Study. *Chem. Mater.* **2010**, *22* (24), 6692−6710.
(22) Leventis, N.; Sotiriou-Leventis, C.; Saeed, A. M.; Donthula, S.; Majedi Far, H.; Rewatkar, P. M.; Kaiser, H.; Robertson, J. D.; Lu, H.; Churu, G. Nanoporous Polyurea from a Triisocyanate and Boric Acid: A Paradigm of a General Reaction Pathway for Isocyanates and Mineral Acids. *Chem. Mater.* **2016**, *28* (1), 67−78.
(23) Chriti, D.; Raptopoulos, G.; Papastergiou, M.; Paraskevopoulou, P. Millimeter-Size Spherical Polyurea Aerogel Beads with Narrow Size Distribution. *Gels* **2018**, *4* (3), 66.
(24) Wu, C.; Taghvaee, T.; Wei, C.; Ghasemi, A.; Chen, G.; Leventis, N.; Gao, W. Multi-Scale Progressive Failure Mechanism and Mechanical Properties of Nanofibrous Polyurea Aerogels. *Soft Matter* **2018**, *14* (38), 7801−7808.
(25) Chidambareswarapattar, C.; McCarver, P. M.; Luo, H.; Lu, H.; Sotiriou-Leventis, C.; Leventis, N. Fractal Multiscale Nanoporous Polyurethanes: Flexible to Extremely Rigid Aerogels from Multifunctional Small Molecules. *Chem. Mater.* **2013**, *25* (15), 3205−3224.
(26) Bang, A.; Buback, C.; Sotiriou-Leventis, C.; Leventis, N. Flexible Aerogels from Hyperbranched Polyurethanes: Probing the Role of Molecular Rigidity with Poly(Urethane Acrylates) Versus Poly(Urethane Norbornenes). *Chem. Mater.* **2014**, *26* (24), 6979−6993.
(27) Donthula, S.; Mandal, C.; Schisler, J.; Leventis, T.; Meador, M. A. B.; Sotiriou-Leventis, C.; Leventis, N. Nanostructure-Dependent Marcus-Type Correlation of the Shape Recovery Rate and the Young's Modulus in Shape Memory Polymer Aerogels. *ACS Appl. Mater. Interfaces* **2018**, *10* (27), 23321−23334.
(28) Papastergiou, M.; Kanellou, A.; Chriti, D.; Raptopoulos, G.; Paraskevopoulou, P. Poly(Urethane-Acrylate) Aerogels via Radical Polymerization of Dendritic Urethane-Acrylate Monomers. *Materials* **2018**, *11* (11), 2249.
(29) Kanellou, A.; Anyfantis, G.; Chriti, D.; Raptopoulos, G.; Pitsikalis, M.; Paraskevopoulou, P. Poly(Urethane-Norbornene) Aerogels via Ring Opening Metathesis Polymerization of Dendritic Urethane-Norbornene Monomers: Structure-Property Relationships as a Function of an Aliphatic Versus an Aromatic Core and the Number of Peripheral Norbornene Moieties. *Molecules* **2018**, *23* (5), 1007.
(30) Papastergiou, M.; Chriti, D.; Damalas, D. E.; Raptopoulos, G.; Paraskevopoulou, P. Poly(Urethane-Acrylate) Aerogels from the Isocyanurate Trimer of Isophorone Diisocyanate. *J. Supercrit. Fluids* **2019**, *148*, 42−54.
(31) Chidambareswarapattar, C.; Xu, L.; Sotiriou-Leventis, C.; Leventis, N.; Skiff, W. M.; Tattershall, C. E.; Kalkan, A. K.; Mang, J. T.; Sotiriou-Leventis, C.; Leventis, N. Robust Monolithic Multiscale Nanoporous Polyimides and Conversion to Isomorphic Carbons. *RSC Adv.* **2013**, *3* (48), 26459−26469.
(32) Leventis, N.; Chidambareswarapattar, C.; Mohite, D. P.; Larimore, Z. J.; Lu, H.; Sotiriou-Leventis, C. Multifunctional Porous

DOI: 10.1021/acsapm.9b00408
ACS Appl. Polym. Mater. 2019, 1, 2322−2333

Aramids (Aerogels) by Efficient Reaction of Carboxylic Acids and Isocyanates. *J. Mater. Chem.* **2011**, *21* (32), 11981−11986.
(33) Saeed, A. M.; Wisner, C. A.; Donthula, S.; Majedi Far, H.; Sotiriou-Leventis, C.; Leventis, N. Reuseable Monolithic Nanoporous Graphite-Supported Nanocatalysts (Fe, Au, Pt, Pd, Ni, and Rh) from Pyrolysis and Galvanic Transmetalation of Ferrocene-Based Polyamide Aerogels. *Chem. Mater.* **2016**, *28* (13), 4867−4877.
(34) Saeed, A. M.; Rewatkar, P. M.; Majedi Far, H.; Taghvaee, T.; Donthula, S.; Mandal, C.; Sotiriou-Leventis, C.; Leventis, N. Selective CO_2 Sequestration with Monolithic Bimodal Micro/Macroporous Carbon Aerogels Derived from Stepwise Pyrolytic Decomposition of Polyamide-Polyimide-Polyurea Random Copolymers. *ACS Appl. Mater. Interfaces* **2017**, *9* (15), 13520−13536.
(35) Lu, H.; Luo, H.; Leventis, N. Mechanical Characterization of Aerogels. In *Aerogels Handbook*; Springer: New York, 2011; pp 499−535.
(36) Ishida, H. Overview and Historical Background of Polybenzoxazine Research. In *Handbook of Benzoxazine Resins*; Ishida, H., Agag, T., Eds.; Elsevier: 2011; pp 3−81.
(37) Lorjai, P.; Chaisuwan, T.; Wongkasemjit, S. Porous Structure of Polybenzoxazine-Based Organic Aerogel Prepared by Sol-gel Process and Their Carbon Aerogels. *J. Sol-Gel Sci. Technol.* **2009**, *52* (1), 56−64.
(38) Lorjai, P.; Wongkasemjit, S.; Chaisuwan, T.; Jamieson, A. M. Significant Enhancement of Thermal Stability in the Non-Oxidative Thermal Degradation of Bisphenol-A/Aniline Based Polybenzoxazine Aerogel. *Polym. Degrad. Stab.* **2011**, *96* (4), 708−718.
(39) Mahadik-Khanolkar, S.; Donthula, S.; Sotiriou-Leventis, C.; Leventis, N. Polybenzoxazine Aerogels. 1. High-Yield Room-Temperature Acid-Catalyzed Synthesis of Robust Monoliths, Oxidative Aromatization, and Conversion to Microporous Carbons. *Chem. Mater.* **2014**, *26* (3), 1303−1317.
(40) Mahadik-Khanolkar, S.; Donthula, S.; Bang, A.; Wisner, C.; Sotiriou-Leventis, C.; Leventis, N. Polybenzoxazine Aerogels. 2. Interpenetrating Networks with Iron Oxide and the Carbothermal Synthesis of Highly Porous Monolithic Pure Iron(0) Aerogels as Energetic Materials. *Chem. Mater.* **2014**, *26* (3), 1318−1331.
(41) Leventis, N.; Palczer, A.; McCorkle, L.; Zhang, G.; Sotiriou-Leventis, C. Nanoengineered Silica-Polymer Composite Aerogels with No Need for Supercritical Fluid Drying. *J. Sol-Gel Sci. Technol.* **2005**, *35* (2), 99−105.
(42) Silverstein, R. M.; Webster, F. X.; Kiemle, D. J. *Spectrometric Identification of Organic Compounds*; John Wiley & Sons: 2005.
(43) Taghvaee, T.; Donthula, S.; Rewatkar, P. M.; Majedi Far, H.; Sotiriou-Leventis, C.; Leventis, N. K -Index: A Descriptor, Predictor, and Correlator of Complex Nanomorphology to Other Material Properties. *ACS Nano* **2019**, *13* (3), 3677−3690.
(44) Leventis, N.; Chidambareswarapattar, C.; Bang, A.; Sotiriou-Leventis, C. Cocoon-in-Web-Like Superhydrophobic Aerogels from Hydrophilic Polyurea and Use in Environmental Remediation. *ACS Appl. Mater. Interfaces* **2014**, *6* (9), 6872−6882.
(45) G'Sell, C. Plastic Deformation of Glassy Polymers: Constitutive Equations and Macromolecular Mechanisms. In *Strength of Metals and Alloys (ICSMA 7)*; Pergamon, 1986; pp 1943−1982.
(46) Timoshenko, S.; Goodier, J. N. *Theory of Elasticity*; McGraw-Hill Book Co.: 1934.
(47) Ferry, J. D. *Viscoelastic Properties of Polymers*; Wiley: 1980.
(48) Churu, G.; Zupančič, B.; Mohite, D.; Wisner, C.; Luo, H.; Emri, I.; Sotiriou-Leventis, C.; Leventis, N.; Lu, H. Synthesis and Mechanical Characterization of Mechanically Strong, Polyurea-Crosslinked, Ordered Mesoporous Silica Aerogels. *J. Sol-Gel Sci. Technol.* **2015**, *75* (1), 98−123.
(49) Mougel, C.; Garnier, T.; Cassagnau, P.; Sintes-Zydowicz, N. Phenolic Foams: A Review of Mechanical Properties, Fire Resistance and New Trends in Phenol Substitution. *Polymer* **2019**, *164*, 86−117.
(50) Lu, X.; Arduini-Schuster, M. C.; Kuhn, J.; Nilsson, O.; Fricke, J.; Pekala, R. W. Thermal Conductivity of Monolithic Organic Aerogels. *Science* **1992**, *255* (5047), 971−972.
(51) Chriti, D.; Raptopoulos, G.; Anyfantis, G. C.; Paraskevopoulou, P. An Extreme Case of Swelling of Mostly cis-Polydicyclopentadiene by Selective Solvent Absorption - Application in Decontamination and Environmental Remediation. *ACS Appl. Polym. Mater.* **2019**, *1*, 1648−1659.
(52) Mohite, D. P.; Mahadik-Khanolkar, S.; Luo, H.; Lu, H.; Sotiriou-Leventis, C.; Leventis, N. Polydicyclopentadiene Aerogels Grafted with PMMA: I. Molecular and Interparticle Crosslinking. *Soft Matter* **2013**, *9*, 1516−1530.
(53) Mohite, D. P.; Mahadik-Khanolkar, S.; Luo, H.; Lu, H.; Sotiriou-Leventis, C.; Leventis, N. Polydicyclopentadiene Aerogels Grafted with PMMA: II. Nanoscopic Characterization and Origin of Macroscopic Deformation. *Soft Matter* **2013**, *9*, 1531−1539.
(54) Leventis, N.; Sadekar, A.; Chandrasekaran, N.; Sotiriou-Leventis, C. Click Synthesis of Monolithic Silicon Carbide Aerogels from Polyacrylonitrile-Coated 3D Silica Networks. *Chem. Mater.* **2010**, *22*, 2790−2803.
(55) Vareda, J. P.; Lamy-Mendes, A.; Durães, L. A Reconsideration on the Definition of the Term Aerogel based on Current Drying Trends. *Microporous Mesoporous Mater.* **2018**, *258*, 211−216.
(56) Du, A.; Zhou, B.; Zhang, Z.; Shen, J. A Special Material or a New State of Matter: A Review and Reconsideration of the Aerogel. *Materials* **2013**, *6*, 941−968.
(57) Si, Y.; Yu, J.; Tang, X.; Ge, J.; Ding, B. Ultralight Nanofibre-Assembled Cellular Aerogels with Superelasticity and Multifunctionality. *Nat. Commun.* **2014**, *5*, 5802 DOI: 10.1038/ncomms6802.
(58) Qian, Z.; Wang, Z.; Zhao, N.; Xu, J. Aerogels Derived from Polymer Nanofibers and Their Applications. *Macromol. Rapid Commun.* **2018**, *39*, 1700724.

DOI: 10.1021/acsapm.9b00408
ACS Appl. Polym. Mater. 2019, 1, 2322−2333